

TECHNICAL MEMORANDUM

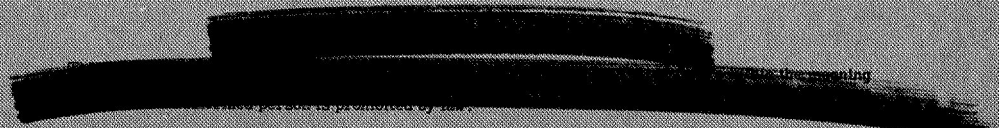
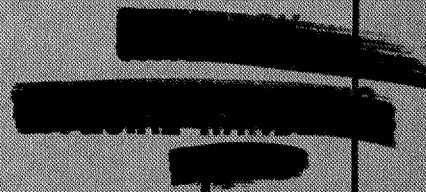
X-783

Declassified by authority of NASA
Classification Change Notices No. 113
Dated ** 6/28/67

PRESSURE AND HEAT-TRANSFER DISTRIBUTION ON THE
AFTERBODY OF A LIFTING MERCURY-TYPE CAPSULE
AT MACH NUMBER 15 IN HELIUM

By Joseph G. Marvin

Ames Research Center
Moffett Field, Calif.



NATIONAL AERONAUTICS AND SPACE ADMINISTRATION
WASHINGTON

April 1963



TECHNICAL MEMORANDUM X-783

PRESSURE AND HEAT-TRANSFER DISTRIBUTION ON THE
AFTERBODY OF A LIFTING MERCURY-TYPE CAPSULE
AT MACH NUMBER 15 IN HELIUM*

By Joseph G. Marvin

SUMMARY

Afterbody pressure and heat-transfer distributions, shock-wave shapes, and photographs of local flow conditions were obtained on a capsule configuration capable of a lifting entry. The test body consisted of a segment of a sphere attached to a rear-facing conical afterbody with a cone angle of 53° . The sphere radius was equal to the maximum body diameter. Data were obtained at Mach number 15 in helium at a Reynolds number based on maximum body diameter of 1.5×10^6 and over an angle-of-attack range from 0° to 30° .

The flow over the windward side of the afterbody changed from separated to attached with increasing angle of attack. At zero angle of attack, the heat-transfer coefficients agreed with a prediction for laminar separated flow obtained when measured surface pressures were used to determine local flow conditions. A heat-transfer coefficient peak on the windward side of the afterbody moved from the most rearward point on the afterbody toward the shoulder with increasing angle of attack.

A method was developed to correlate heat-transfer rates measured in helium with those obtained in air. The method is used to compare wind-tunnel results with heating rates measured on the Mercury MA5 flight.

INTRODUCTION

Aerodynamic lift on a capsule entering the earth's atmosphere has well-known advantages and can be achieved with a Mercury type capsule by trimming it at angle of attack. (See refs. 1 and 2.) However, wind-tunnel measurements indicate that the maximum heating rates on the conical afterbody of the Mercury capsule increase from about 2 to 20 percent of the stagnation value as the capsule attitude changes from 0° to 20° angle of attack. (See ref. 3.) The

afterbody is surrounded by wake and separated flows and extensive wind-tunnel and flight test will be required to determine the real nature of the afterbody flow and to make possible a general analytical treatment which will allow minimum weight thermal protection systems to be achieved. The purpose of the present tests was: (1) to obtain afterbody pressures and heat-transfer data at higher Mach numbers than have previously been attained and to compare the results with theory; (2) to obtain some knowledge of the extent of flow separation at angles of attack and its subsequent effect on heat transfer; (3) to compare these heat-transfer results obtained in helium with data obtained in air, and to extend and compare the wind-tunnel results to actual flight conditions.

SYMBOLS

C	thermal capacitance per unit area of test body wall
c_p	specific heat at constant pressure
c_v	specific heat at constant volume
D	maximum body diameter
h	heat-transfer coefficient, $\frac{q_w}{T_r - T_w}$
$\frac{h}{h_0, a=0}$	ratio of local heat-transfer coefficient to the stagnation point heat-transfer coefficient at zero angle of attack
H	fluid enthalpy, $c_p T$
$\frac{H_r}{H_0}$	ratio of the enthalpy evaluated at the recovery temperature and surface pressure to the enthalpy evaluated at the stagnation point temperature and pressure
k	fluid thermal conductivity
M	Mach number
Nu_D	Nusselt number based on maximum body diameter, $\frac{hD}{k}$
Nu_x	Nusselt number based on length of boundary-layer run, $\frac{hx}{k}$
Pr	Prandtl number, $\frac{c_p \mu}{k}$
p	pressure
$\frac{p}{p_{t_2}}$	ratio of afterbody surface pressure to impact pressure at the free-stream Mach number

q	heat-transfer rate normal to the body surface per unit area
R	one-half the maximum body diameter
Re	Reynolds number per unit length, $\frac{\rho U}{\mu}$
Re_x	Reynolds number based on length of boundary-layer run, $\frac{\rho U x}{\mu}$
Re_D	Reynolds number based on maximum body diameter, $\frac{\rho U D}{\mu}$
S	distance along the body surface measured from the stagnation point with the body at zero angle of attack
St	Stanton number, $\frac{h}{\rho U c_p}$
T	temperature
T'	reference enthalpy temperature
U	fluid velocity
\bar{U}	ratio of flight velocity to entry velocity
x	length of boundary-layer run
X, Y	coordinates defined in figure 1
α	angle of attack measured between the axis of symmetry and the free-stream vector
γ	ratio of fluid specific heats, $\frac{c_p}{c_v}$
t	time
μ	fluid viscosity
ρ	fluid density
ϕ	azimuth angle as defined in figure 1
ψ	the difference in angle between the free-stream direction and upper meridian of the afterbody surface
ω	exponent on power law variation for viscosity
(\prime)	properties evaluated at the reference enthalpy temperature, T'

A	air
H	helium
o	stagnation-point value
r	evaluated at recovery temperature
t	total conditions (i.e., conditions that would exist if the gas were brought to rest isentropically)
w	evaluated at the wall
2	conditions behind a normal shock wave
w	free-stream value

APPARATUS

Tunnel

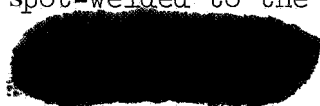
The tests were conducted in the Ames Hypersonic Helium Tunnel at a free-stream Mach number of 15 and a free-stream Reynolds number of 0.74×10^6 per inch. Nominal operating total temperature and pressure were 545°R and 1200 psia. This facility is a blowdown tunnel equipped with an axisymmetric contoured nozzle and a 20-inch diameter test section. For a complete description of this facility see reference 2.

Instrumentation

All data were recorded on magnetic tape by a Beckman Model 210 high-speed recording system, also described in reference 2.

Static pressures on the model surface were measured with vibrating diaphragm pressure cells. These cells measure pressure over a wide range by sensing the damping characteristics of a vibrating diaphragm immersed in the test gas. A description of this cell is given in reference 4. The cells used had a pressure range from approximately 10^{-1} to 30 mm Hg with a maximum error of ± 5 percent of reading over the full range. To shorten the pressure tubing to the model, the pressure cells were located in the model support. Between test runs, the pressure cells were connected to a vacuum chamber in order to prevent contamination by condensable vapors.

Model surface temperatures were obtained from the emf output of 40 gage chromel-constantan thermocouples spot-welded to the inside of a thin-shelled



test model. Individual temperatures were recorded every 0.2 seconds. The precision of the temperature measurements was $\pm 1^\circ \text{F}$.

Model

Details of the model and instrumentation locations are shown in figure 1. The model consisted of a segment of a sphere attached to a rear-facing conical afterbody with a cone angle of 53° . The sphere radius is equal to the maximum body diameter.

Stainless steel models were used for the pressure and heat-transfer tests. The heat-transfer model wall thicknesses were 0.125 and 0.017 inch for the forebody and the conical afterbody, respectively. These relative thicknesses were chosen in an attempt to achieve isothermal temperature conditions over the entire body during the data gathering portion of the transient heat-transfer tests. The pressure and heat-transfer models were mounted on an offset sting, as shown in figure 2(a), in an attempt to minimize interference between the sting and the flow over the afterbody. All instrumentation in the afterbody was confined to the section of the model opposite the sting support. The sting and model were rotated in the support strut to obtain data at different azimuth angles.

A third model used for afterbody flow visualization tests is shown in figure 2(b). This model was brass and was mounted on a vertical Bakelite strut. The upper portion of the strut was removable, and additional inserts were used to vary the angle of attack.

TEST METHOD

Pressure Tests

Prior to each pressure test run, the vibrating diaphragm pressure cells were connected to a bell jar and calibrated in a helium atmosphere. After calibration, they were connected to the model and the test section was evacuated and purged with helium to assure that helium gas filled the cells and related tubing. The tunnel was started with the model at zero angle of attack. After supersonic flow was established, the model was positioned at the desired angle of attack and kept there until a constant value of pressure was recorded by the measuring cells. During each test run, data could usually be taken at two angles of attack.

Heat-Transfer Tests

Heat-transfer data were obtained by a transient temperature technique. Before each run the heat-transfer model was heated or cooled with nitrogen gas. The nitrogen gas was passed through the rear of the temperature control probe

(fig. 2(a)) and over the outer surface of the model. The range of model afterbody temperatures during these tests was $0.8 < T_w/T_t < 1.1$. The tunnel was started with the temperature control probe in front of the model. When supersonic flow was established, the probe was raised to the top of the test section, and then the model was positioned at the desired angle of attack. This sequence of operations took less than 0.5 second. The model remained nearly isothermal through the data gathering period (1 sec). The temperature difference between adjacent thermocouples never exceeded 10°R and in most instances was less. The measured wall temperatures were used to estimate skin-conduction heating rates which were found to be negligible compared to the convective heating rates.

Heat-Transfer Data Reduction

Normally, the heat-transfer rate through the model wall, neglecting conduction and radiation terms, can be related to the aerodynamic heat-transfer rate by the following equation taken from reference 5:

$$q_w = c \frac{dT}{d\theta} = h(T_r - T_w) \quad (1)$$

For the present tests, however, equation (1) was modified to account for small changes in total pressure and temperature which occurred during the initial portion of the heat-transfer test runs. In order to introduce total temperature and pressure into equation (1), the following method was used. Over the afterbody, the heat transfer was assumed to behave in a manner similar to that within a two-dimensional laminar boundary layer. Equation (1) was rewritten as:

$$q_w = St_\infty \sqrt{Re_\infty} (\rho_\infty U_\infty \mu_\infty)^{1/2} c_{p_\infty} \left(\frac{T_r}{T_t} - \frac{T_w}{T_t} \right) T_t \quad (2)$$

The T^* method and modified Reynolds analogy along with a power law variation for viscosity were used to obtain:

$$St_\infty \sqrt{Re_\infty} = \frac{K_1}{Pr^{2/3}} \left(\frac{T_\infty}{T^*} \right)^{\frac{1-\omega}{2}} \quad (3)$$

Substitution of equation (3) with $\omega = 0.647$ for helium changes equation (2) to

$$\frac{q_w}{T_t^{1.074} p_t^{1/2}} = \frac{K_2}{Pr^{2/3}} \left(\frac{T_t}{T^*} \right)^{0.177} c_{p_\infty} \left(\frac{T_r}{T_t} - \frac{T_w}{T_t} \right) F(M_\infty) \quad (4)$$

where K_1 and K_2 are constants and $F(M_\infty)$ contains the terms T/T_t and p/p_t . For small changes in total pressure and temperature, equation (4) can be approximated by:



$$\frac{q_w}{T_t p_t^{1/2}} = K_3 \left(\frac{T_r}{T_t} - \frac{T_w}{T_t} \right) \quad (5)$$

It can be shown that equation (5) also applies for stagnation point flows. Comparison of equations (1) and (5) shows that K_3 is the heat-transfer coefficient (h) divided by the square root of the total pressure. During the present series of tests, the ratios of maximum to minimum total pressure and temperature for a single run were never larger than 1.03 and 1.10, respectively. In light of the small variation in total pressure, it was expected that K_3 would be a constant for any given run. Equation (5) was used to obtain local recovery temperature and heat-transfer coefficients.

Representative heating-rate data are presented in figure 3 for the stagnation point and for a typical afterbody station. In this figure, data at different initial wall temperatures are plotted in the form given by equation (5) to illustrate the data-reduction technique. The heat-transfer rate was evaluated by differentiating the time-temperature history by a variational differencing technique programmed on an IBM 7090 computer. The recovery or adiabatic wall temperature is defined as the wall temperature for zero heat-transfer rate. As shown in figure 3(a), the stagnation-point recovery temperature was equivalent to the free-stream stagnation temperature. This, along with the fact that the data assume a linear variation with T_w/T_t , tends to verify experimentally the form given by equation (5).

Flow Visualization

Two methods were used to obtain information on the shock-wave shape and afterbody flow. Shadowgraphs of the model and shock-wave system were taken over the complete range of angles of attack during the pressure test runs. Shock-wave shapes were measured from these shadowgraphs. Details of the afterbody flow were obtained by utilizing a glow discharge between a specially constructed model and a grounding electrode. The direct-current potential of the electrically isolated model was increased until glow was established between the model and a grounding electrode. The electrode was located far enough from the model to insure that any disturbances originating from the probe did not interfere with the flow over the afterbody.

RESULTS AND DISCUSSION

Flow Visualization

Shadowgraphs and afterbody glow photographs are presented to give a composite picture of the flow over the test body. The orientation of the bow shock wave with respect to the model at various angles of attack is shown in the shadowgraphs of figure 4. In general, with increasing angle of attack, the shock



[REDACTED]

wave over the windward side of the model and in the vicinity of the stagnation point moves toward the body and becomes more curved. The measured shock-wave shapes for the complete range of angles of attack are presented in figure 5. The coordinate system used here is defined in figure 1.

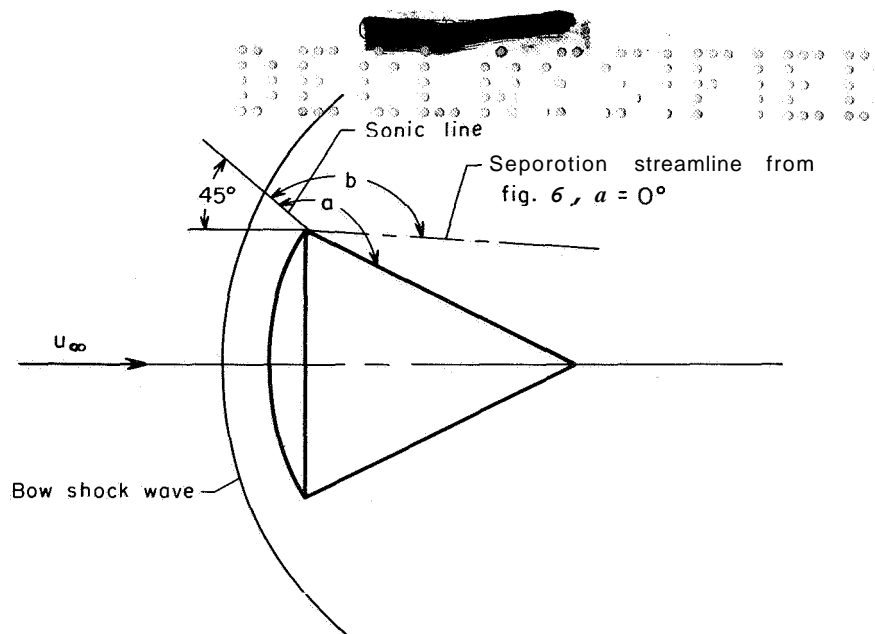
The flow over the afterbody, as obtained from the glow-discharge technique, is shown in figure 6. The white regions outside the model silhouettes are believed to be separated flow regions. While there is no definite evidence of this, the changes in these regions resulting from changing the model angle of attack appear to support this interpretation. Later in the report, a comparison of the regions of flow separation and reattachment as indicated in the photographs and as indicated by pressure and heat-transfer data also tend to support this interpretation. The high intensity spots on the afterbody surface are corona discharges and appear to have no physical meaning with regard to the flow over the body. If the above interpretation of the white regions is correct, then definite flow separation regions exist over the entire afterbody at 0° and 10° angle of attack, and at least over the leeward side for the larger angles. On the most windward side at 15° angle of attack, the flow appears to attach near the end of the cone, and at 20° , the attachment moves farther upstream until at $26\frac{1}{2}^\circ$ the flow is completely attached.

Pressure Distribution

It is of interest to examine the measured surface pressures to see whether the separated and attached regions indicated by the flow visualization can be identified. In addition, the measured pressures will be compared with various theoretical predictions.

Figure 7 presents the normalized measured surface pressures on the most windward meridian of the test body plotted against the normalized distance along the body surface. The pressures on the afterbody decreased slightly as angle of attack was increased up to 10° . Further increases in angle of attack caused the maximum afterbody pressure to increase and move from a rearward position on the body toward the shoulder.

To obtain a better understanding of the conditions of the flow over the afterbody, the pressure for attached and separated flow at zero angle of attack estimated by two-dimensional Prandtl-Meyer theory is included in figure 7. The assumed expansion angles (see sketch (a)) are $a - \pi/2$ for attached flow and $b - \pi/2$ for separated flow. The straight sonic line was assumed to extend from the model corner forward to the shock wave at an angle of 45° with the free-stream velocity vector. These assumptions and their limitations were discussed in reference 6. The comparison of Prandtl-Meyer theory and measured surface pressures at zero angle of attack indicates that the flow over the afterbody is separated and substantiates the interpretation of the flow visualization pictures. Also, the comparison seems to lend some justification for the simplifying assumptions involved in applying the theory. As pointed out in reference 6,



Sketch (a)

three-dimensional flow theory predicts only slightly lower surface pressures than these calculated for two-dimensional flow, and, hence, has not been shown in the present comparison.

With increasing angle of attack, the afterbody glow photographs indicate that reattachment did occur and the pressure data seem to substantiate this conclusion. The dashed curve in figure 7 is the reattachment pressure estimated by the two-dimensional theory given in reference 7, and is in fair agreement with the maximum pressures measured on the afterbody at 20° angle of attack. In the application of theory, the total pressure along the separation streamline was assumed to be the reattachment static pressure. For angles of attack greater than 20° , the lower pressure near the corner, resulting from expansion of the flow around the corner, followed by a higher pressure is characteristic of attached flow. (See, e.g., the data of ref. 8.)

In figure 8 the normalized surface pressures on the afterbody are plotted against azimuth angle for fixed distances along the afterbody and over a range of angles of attack. In general, on the windward side of the afterbody, the pressures increase with increasing angle of attack. For a given angle of attack, the pressures decrease from a maximum value on the most windward meridian to about the zero angle of attack value on the most leeward meridian.

It appears that the flow visualization and pressure studies define the regions of flow separation and reattachment rather well.

Heat Transfer

It is informative to examine the heat-transfer rates measured on the afterbody, to show the subsequent effect of separation on heat transfer, and to compare the measured results with theory.

CONFIDENTIAL

Figure 9 presents the measured normalized heat-transfer coefficients on the most windward meridian plotted against the normalized distance along the body surface for a range of angles of attack. The general trend of the heat-transfer data with angle of attack follows that of the surface pressure data. The data show an increase in heat transfer with increasing angle of attack. A peak value of the heat-transfer coefficient moves toward the shoulder with increasing angle of attack.

In figures 9(a) and (b), the measured results are compared with those calculated from laminar flat plate theory. The laminar results have been multiplied by 0.56, the ratio of average separated flow heat transfer to attached flow heat transfer, as given in reference 9. Local flow conditions were obtained by assuming an isentropic expansion from the impact pressure to the measured surface pressures. These theoretical estimates were based on a boundary-layer length of run beginning at the stagnation point. All fluid properties were evaluated at a temperature given by Eckert's reference enthalpy method (ref. 10). Despite the simplicity of this approach, good agreement between theory and measurement was obtained at 0° angle of attack. At 15° angle of attack agreement between the level of the theory and measurement is adequate for S/R around 1.5. The high heat-transfer coefficient just downstream of the shoulder is believed to be caused by the local increase in velocity of the fluid being scavenged from the separation region (see ref. 9).

The flow visualization and pressure studies indicated reattachment occurred about midway on the afterbody at 20° angle of attack; hence, for the angles above 15° , comparison with attached laminar flat plate theory is made. In applying the theory, the length of boundary-layer run was measured along the surface from the most forward point on the spherical forebody and, therefore, varied with angle of attack. The theory does not give an adequate representation of the data. Transition to turbulent flow was not considered since estimates of local Reynolds number were below those normally associated with turbulent flow, and since the increases in heat transfer with S/R and angle of attack appear to be directly related to increases in pressure (cf. figs. 7 and 9). At these angles of attack, the unsymmetrical nature of the flow may affect the comparison. It is believed that the crossflow caused by the pressure decay around the circumference of the body (see figs. 8(a) and (c)) causes a significant increase in heat transfer. It is of interest that no abrupt local increase in heat transfer occurred at 20° angle of attack where flow visualization and pressure measurements indicated flow reattachment. This seems to indicate that the flow reattaches at a small angle of inclination to the afterbody surface.

In figure 10, the normalized heat-transfer coefficients are plotted against azimuth angle for fixed distances along the afterbody and for angles of attack up to 30° . Generally, this figure shows that for a given position on the windward side of the afterbody, the heat-transfer coefficients increase with increasing angle of attack. Around the circumference, the heat-transfer coefficients decrease from a maximum on the most windward meridian ($\phi = 0^\circ$) to the zero angle of attack value on the most leeward meridian ($\phi = 180^\circ$). The heat-transfer data in figure 10 follow the same general pattern as the pressure distribution data in figure 8. It seems reasonable to assume that the regions of separated flow

are those where the heat-transfer is about equal to the zero angle of attack value. For example, at 26-172° angle of attack, only flow over the leeward side of the model is separated.

Comparison of Air-Helium Data

It is of interest to compare the present afterbody heat-transfer data with data obtained in air on a similar configuration. This comparison is useful as a means for evaluating the present results and also may suggest a means for extrapolating wind-tunnel data to flight conditions.

In figure 11(a), the present heat-transfer data are compared with air data on the conical afterbody of the Mercury configuration from references 11 and 12. To account for the difference in conical afterbody angles, the data are compared on the basis of the angle (γ) which the free stream makes with the afterbody surface. (See fig. 1(a).) (For those cases where air and helium data were not available at identical values of γ , a comparison is made between sets of data at approximately the same γ .) The data compare favorably when the two bodies are at zero angle of attack, but agree less favorably at the higher angles of attack.

Differences between the heat transfer for air and helium might be expected because of a number of effects, in addition to the basic difference in the test gases. For example, the model configurations in figure 11(a) were different (26-1/2° and 20° afterbody angle, a continuous conical afterbody compared with a cone cylinder); the Reynolds numbers and Mach numbers were different; the tests were conducted in different wind tunnels and somewhat different data gathering and analysis techniques were used. The above-mentioned differences mainly influence the local flow conditions over the model. If local flow conditions could be calculated, adjustments accounting for these differences could be made and could thereby provide a method for comparing helium results with air data. To obtain a basis for comparison, the stagnation-point heating relationship given in reference 13,

$$Nu_{D_2} \sim Pr_2^{1/3} \sqrt{\frac{D}{u_2} \left(\frac{du}{ds} \right)_0} \sqrt{Re_{D_2}} \quad (6)$$

and the Newtonian velocity gradient at the stagnation point for hypersonic flows given in reference 14,

$$\frac{D}{u_2} \left(\frac{du}{ds} \right)_0 = \frac{2(\gamma+1)}{\sqrt{\gamma(\gamma-1)}} \quad (7)$$

were combined with the relationship used for obtaining the separated flow theory in figure 9(a),

$$Nu'_x \sim (Pr')^{1/3} \sqrt{Re'_x} \quad (8)$$

to obtain the following equation:

$$\left(\frac{h}{h_{O, \alpha=0}}\right)_A = \left(\frac{h}{h_{O, \alpha=0}}\right)_H \left\{ \frac{(\gamma+1)_A [\gamma(\gamma-1)]_A^{1/2} Re'_A (Re_2)_H (x/D)_H}{(\gamma+1)_H [\gamma(\gamma-1)]_H^{1/2} Re'_H (Re_2)_A (x/D)_A} \right\}^{1/2} \left[\frac{(Pr_2)_A (Pr')_H}{(Pr_2)_H (Pr')_A} \right]^{2/3} \frac{(\mu' c_p')_A (\mu_2 c_{p_2})_H}{(\mu' c_p')_H (\mu_2 c_{p_2})_A} \quad (9)$$

The subscripts A and H refer to air and helium gases, respectively. Equation (9) can be written for comparison of any two gases or any two different tests in the same gas by appropriate subscript changes. For the data of figure 11(a) only small changes are predicted as is shown in figure 11(b), where equation (9) was used to adjust the present data and those of reference 12. The three sets of data compare about equally well in both parts of figure 11. Although this comparison is inconclusive, it is believed that equation (9) provides a means for correlating wind-tunnel and flight data at least for the lower angles of attack where helium and air data are in agreement. This is illustrated by comparing estimated heating rates from wind-tunnel results with actual flight data. Using the cold-wall approximation, the flight heating-rate ratio can be written as follows:

$$\left(\frac{q}{q_{O, \alpha=0}}\right)_A = \left(\frac{h}{h_O}\right)_A \left(\frac{H_r}{H_O}\right)_A \left(\frac{c_{p_2}}{c_{p'}}\right)_A \quad (10)$$

where the value of $(h/h_O)_A$ is obtained from equation (9) using the subscript A to represent the real-gas quantities as estimated from trajectory information. A comparison of measured heating-rate ratios and estimated ratios using equation (10) for the Mercury MA-5 flight is presented in figure 12. The flight data were obtained by Kenneth Weston and Archie Fitzke of the NASA Manned Spacecraft Center. The agreement of the data at $\phi = 0^\circ$ and $\phi = 160^\circ$ for a station about midway on the conical afterbody indicates that the capsule was at small angle of attack. The heating-rate ratio is plotted against \bar{u} , the ratio of flight velocity to entry velocity. Two estimated equilibrium heating-rate ratios are shown: One, obtained by setting the Prandtl number ratio in equation (9) to unity, and the other by using the Prandtl number ratio obtained from the air properties given in reference 15. In order to obtain the flight local flow conditions, thermodynamic equilibrium was assumed and the surface pressure was estimated from the correlation of air wind-tunnel results presented in reference 3. In equation (10), the enthalpy ratio $(H_r/H_O)_A$ was assumed to be 0.87, the experimental value obtained during the present tests at $\alpha = 0^\circ$. The estimated equilibrium heating-rate ratios from equation (10) compare very well with the measured ratios for $0.6 < \bar{u} < 0.95$. The estimates indicate a Mach number independence for values of $\bar{u} < 0.85$. In general, the flight data also exhibit this independence for $0.6 < \bar{u} < 0.85$. The rapid increase in flight heating-rate ratio for $\bar{u} < 0.6$ may reflect transition to turbulent flow or flow reattachment, either of which is not within the scope of equation (10) as applied here.

CONCLUSIONS


A study of the afterbody flow over a capsule entry configuration in helium at Mach number 15 resulted in the following conclusions:

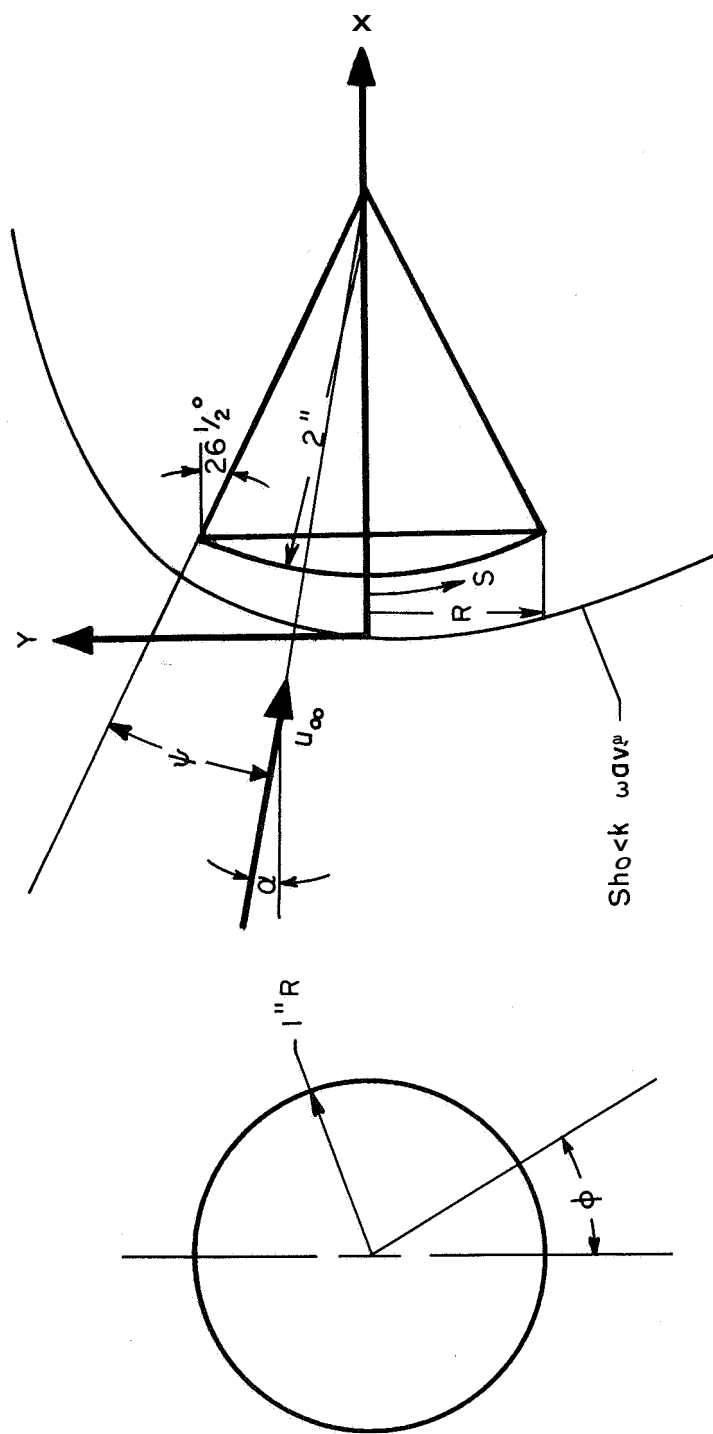
1. At zero angle of attack the flow was separated and laminar separated flow theory predicted the afterbody heat-transfer coefficients.
2. The flow over the windward side of the afterbody changed from separated to attached with increasing angle of attack. As indicated by flow photographs and surface pressures, reattachment occurred on the afterbody at about 20° angle of attack. No sudden increase in heat transfer was found in the zone of reattachment.
3. The helium data correlate; with air data for a similar capsule configuration up to an angle of 10° between the free stream and afterbody surface.
4. A method to adjust heating rate data on the basis of differences in test conditions was found to give an adequate estimate of laminar heating rates during the nonlifting entry of the Mercury capsule MA5 flight.

Ames Research Center
National Aeronautics and Space Administration
Moffett Field, Calif., Oct. 9, 1962

REFERENCES

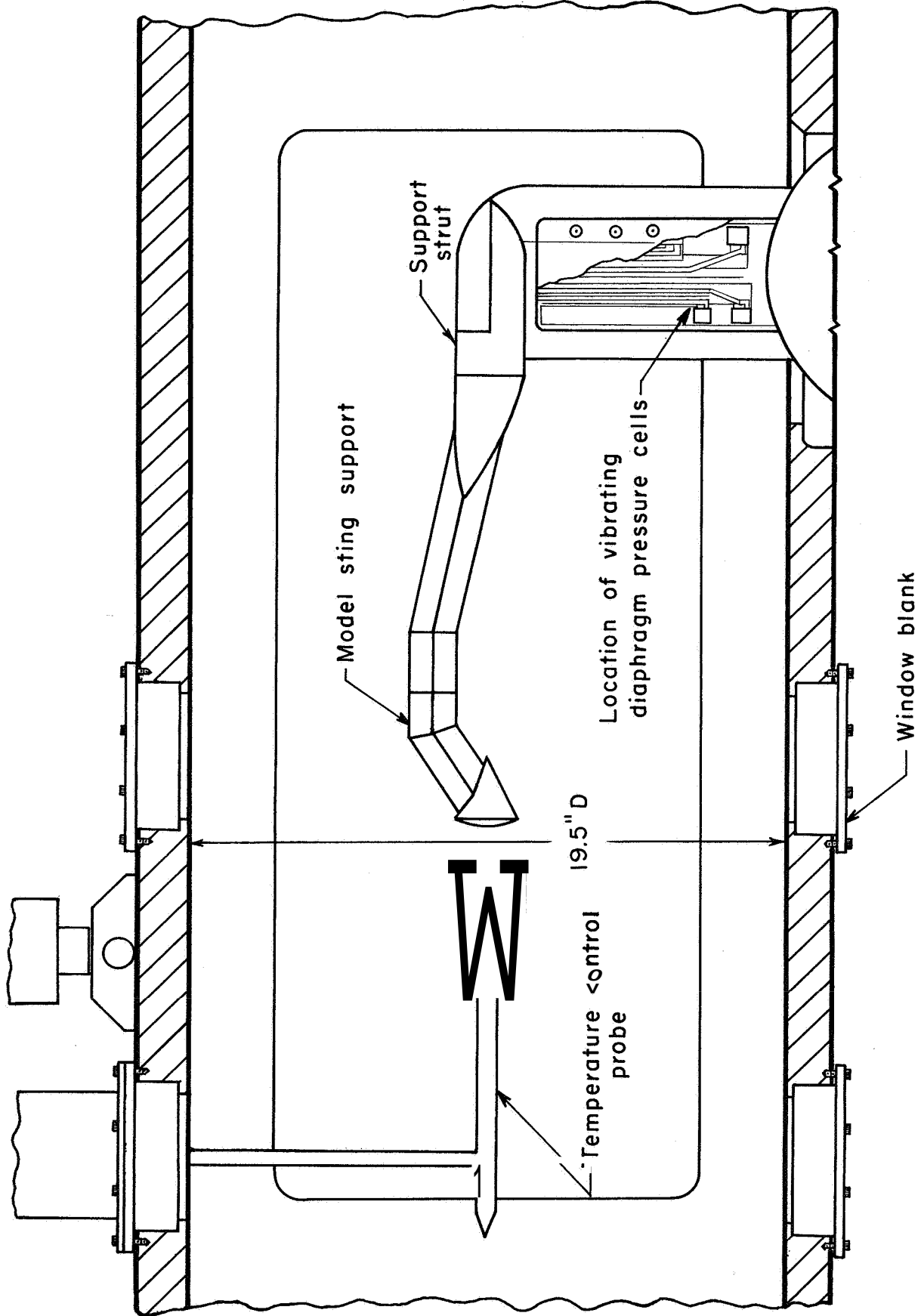
1. Sammonds, Robert I., and Rickey, Robert R.: Effectiveness of Several Control Arrangements on a Mercury-Type Capsule. NASA TM X-579, 1961.
2. Tendeland, Thorval, and Pearson, Byrd D.: Effectiveness of Two Flap Controls on a Mercury Type Capsule at Mach Number of 15 in the Ames Hypersonic Helium Tunnel. NASA TM X-660, 1962.
3. Weston, Kenneth C., and Swanson, Joanna E.: A Compilation of Wind-Tunnel Heat-Transfer Measurements on the Afterbody of the Project Mercury Capsule Reentry Configuration. NASA TM X-495, 1961.
4. Dimeff, John, Lane, James W., and Coon, Grant W.: A New Wide-Range Pressure Transducer. Review of Scientific Instruments, vol. 33, Aug. 1962, pp. 804-811.
5. Marvin, Joseph G.: Surface Pressures and Heat Transfer on Unswept Blunt Plates in Helium at High Mach Numbers. NASA TN D-688, 1961.

- 
6. Reller, John O., Jr., and Seegmiller, H. Lee: Pressure and Heat-Transfer Measurements on a Mercury Capsule Model. NASA TM X-647, 1962.
 7. Chapman, Dean R., Kuehn, Donald M., and Larson, Howard K.: Investigation of Separated Flows in Supersonic and Subsonic Streams With Emphasis on the Effect of Transition. NACA TN 3869, 1957.
 8. Bogdonoff, S. M., and Vas, I. E.: Experimental Studies at Mach Numbers 12 to 19 of Conical and Blunted Bodies at Zero Angle of Attack. Princeton University Rep. 435 (Contract No. AF 18(600)-498) Sept. 1958.
 9. Chapman, Dean R.: A Theoretical Analysis of Heat Transfer in Regions of Separated Flow: NACA TN 3792, 1956.
 10. Eckert, E. R. G.: Engineering Relations for Friction and Heat Transfer to Surfaces in High Velocity Flow. Jour. Aero. Sci. 22, 1955, pp. 585-587.
 11. Pritts, O. R., and Mallard, S. R.: Pressure and Heat-Transfer Distribution on a One-Tenth Scale Mercury Capsule at Mach Number 8. AEDC TN-59-164 (Contract No. AF 40(600)-800) Arnold Eng. Dev. Center, Jan. 1960.
 12. Everhart, Philip E., and Bernot, Peter T.: Measurements of the Surface Flows, Heat Transfer, Pressure Distribution, and Longitudinal Stability of a Mercury Capsule Model at Mach Numbers of 6.9 and 9.6. NASA TM X-458, 1961.
 13. Lees, Lester: Laminar Heat Transfer Over Blunt-Nosed Bodies at Hypersonic Flight Speeds. Jet Propulsion, vol. 26, April 1956, pp. 259-268, 274.
 14. Lees, Lester: Hypersonic Flow. Proc. Fifth International Aeronautical Conference (Los Angeles, Calif., June 20-23, 1955), Inst. Aero. Sci., 1955, pp. 241-276.
 15. Hansen C. Frederick: Approximations for the Thermodynamic and Transport Properties of High-Temperature Air. NASA TR R-50, 1959.



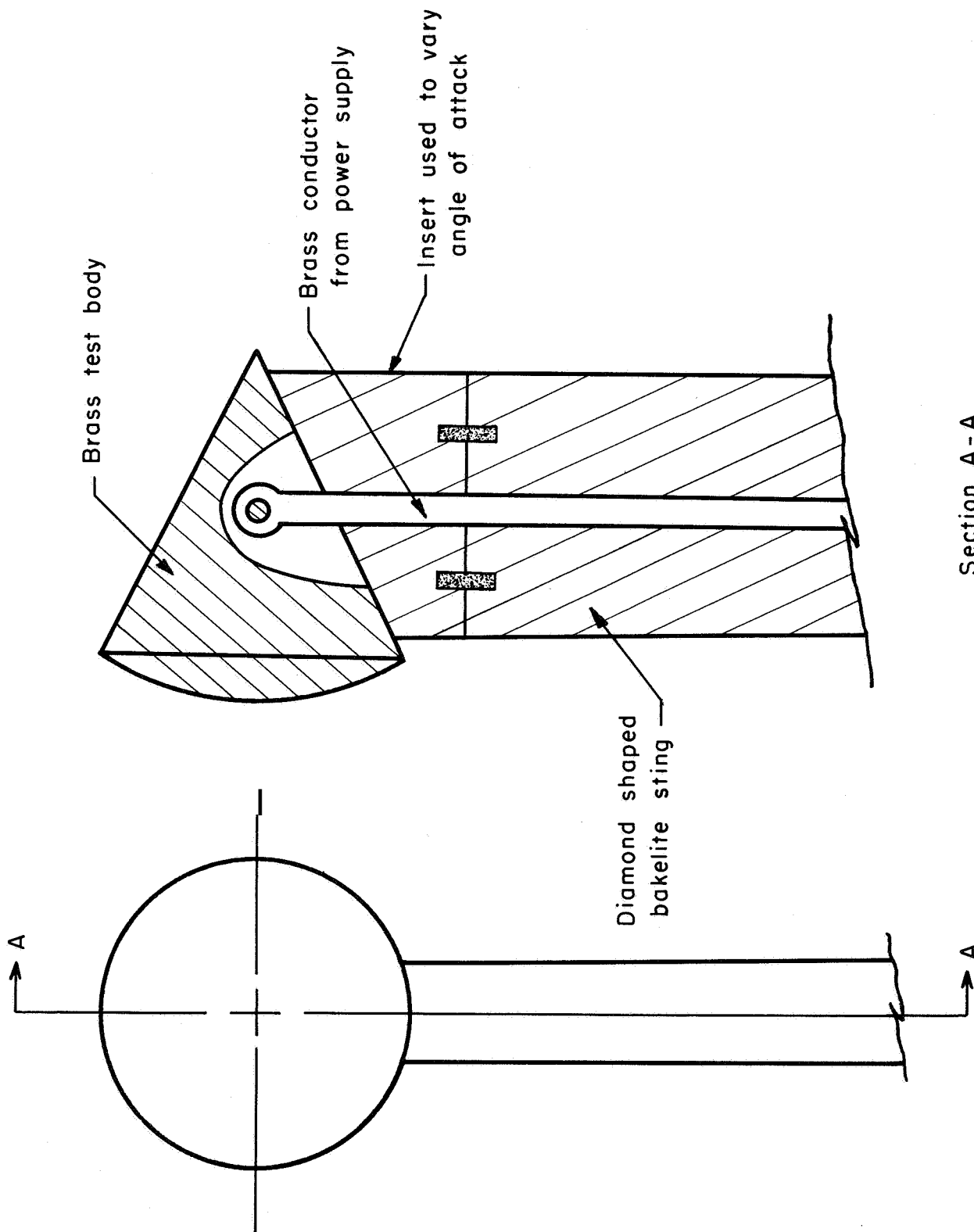
Pressure orifice location		Thermocouple location	
ϕ	$\frac{S}{R}$	ϕ	$\frac{S}{R}$
0,45	1.251	0,45	1.049
	1.651	0,45	1.251
	2.151	0,45	1.424
	2.651	0,45	1.651
		0,45	1.924
		45	2.151
		0,45	2.424
		0,45	2.651
		0,45	2.924

Figure 1.- Model and instrumentation locations.



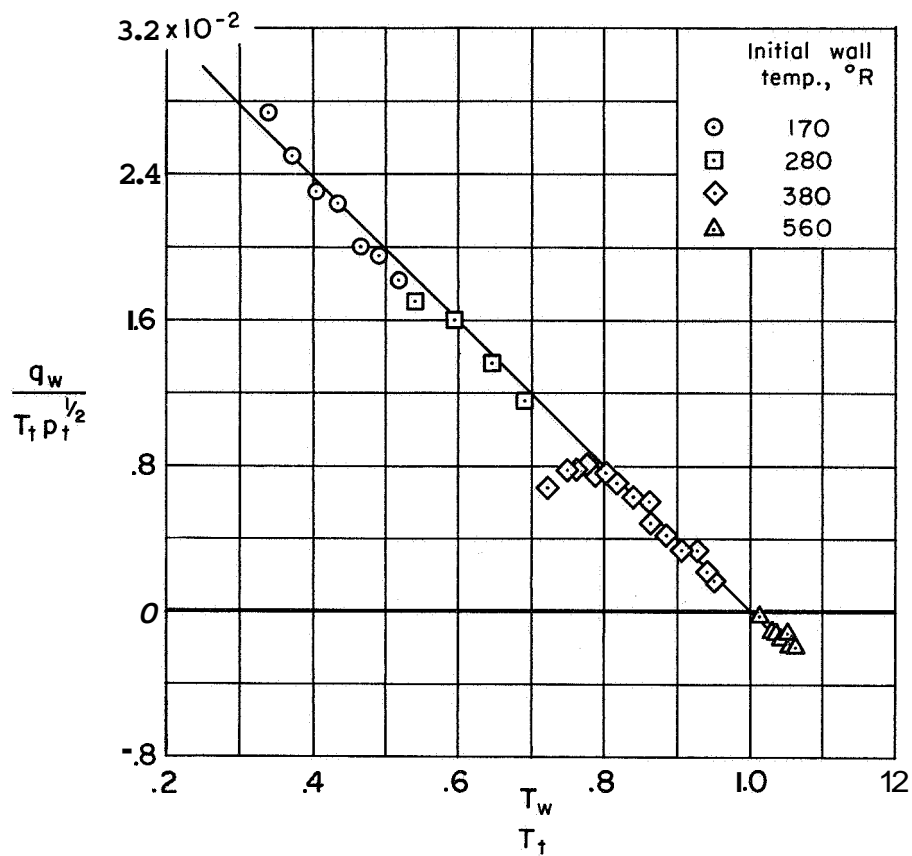
(a) Pressure and heat-transfer models.

Figure 2.- Test-section location and support systems for various models.

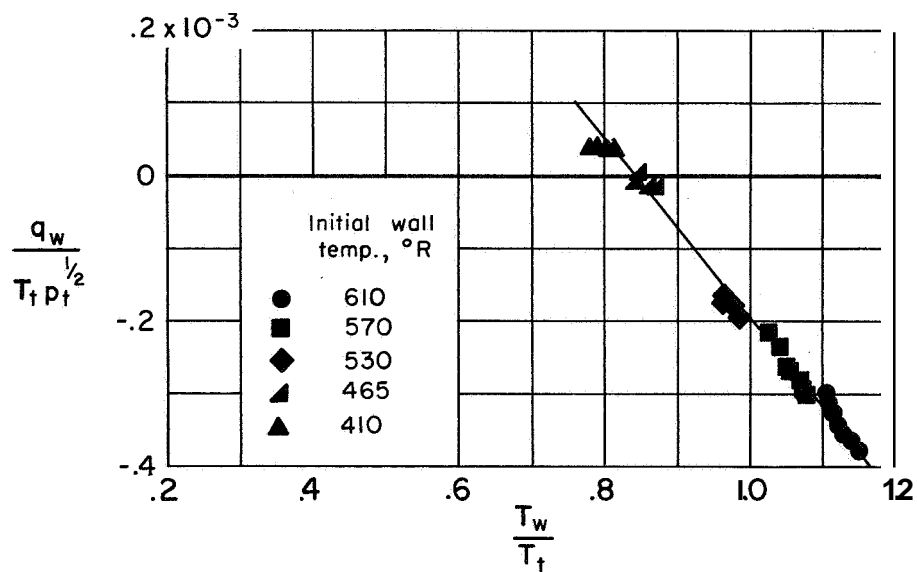


(b) Afterbody flow-visualization model.

Figure 2.- Concluded.



(a) Stagnation point, $\alpha = 0^{\circ}$.



(b) Afterbody, $S/R = 1.651$ and $\alpha = 15^{\circ}$.

Figure 3.- Graphical method for obtaining the recovery temperature and heat-transfer coefficient at the stagnation point and at a position on the afterbody for $\phi = 0^{\circ}$.

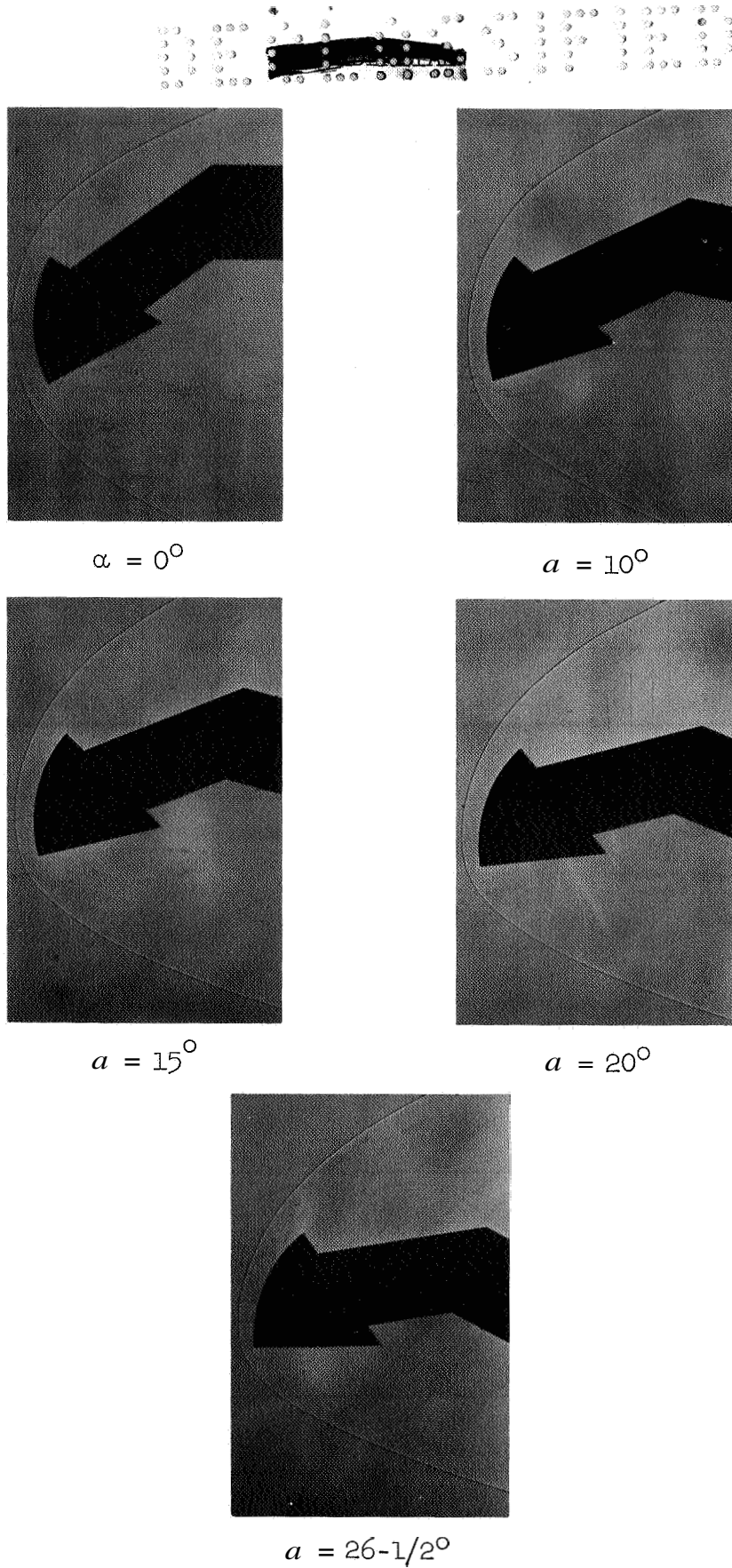
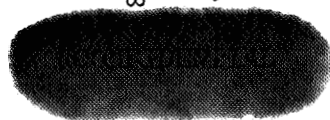


Figure 4.- Shadowgraphs of the shock-wave shapes for various angles of attack at $M_\infty = 15$.



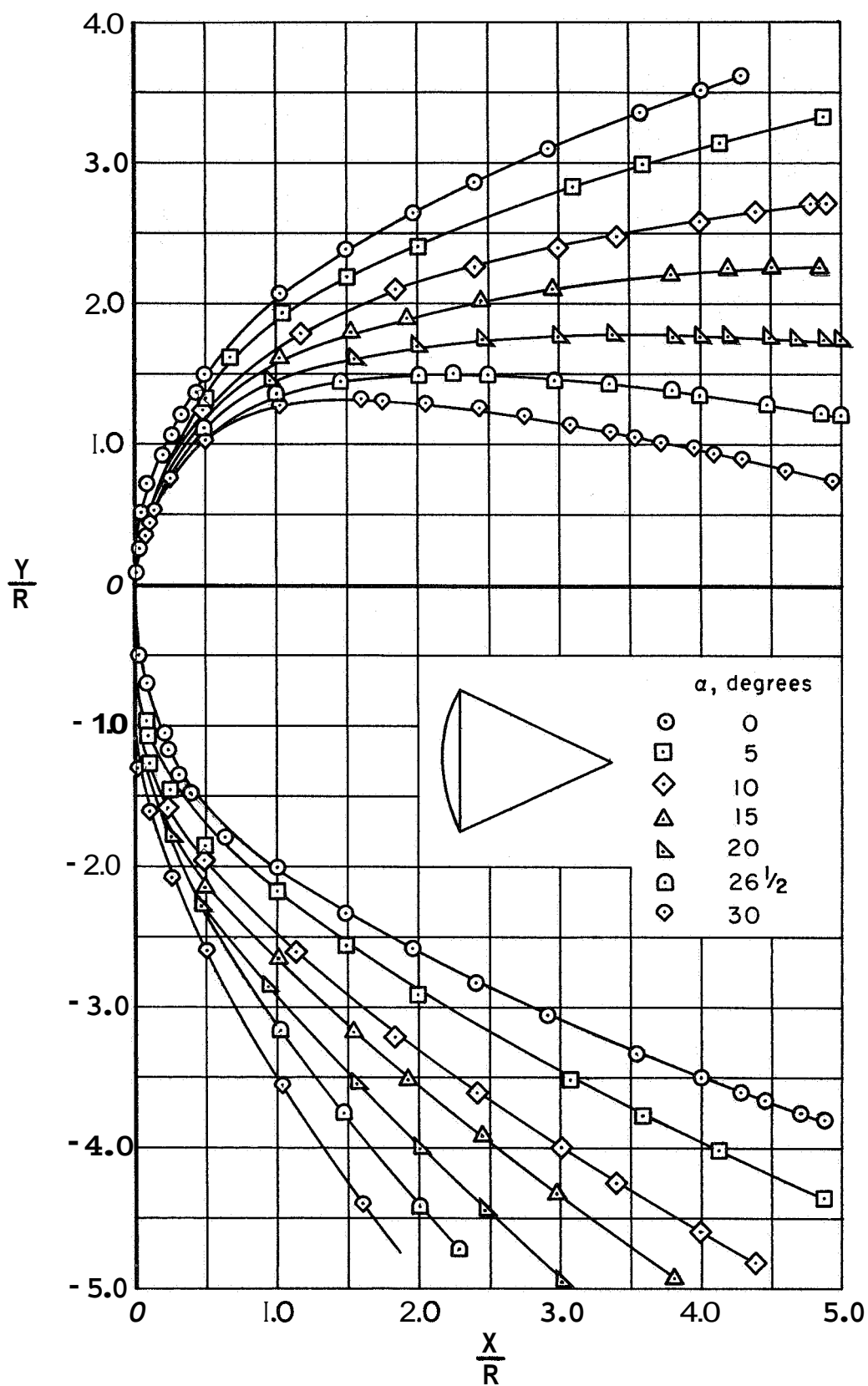


Figure 5.- Measured shock-wave shapes for various angles of attack at $M_\infty = 15$.

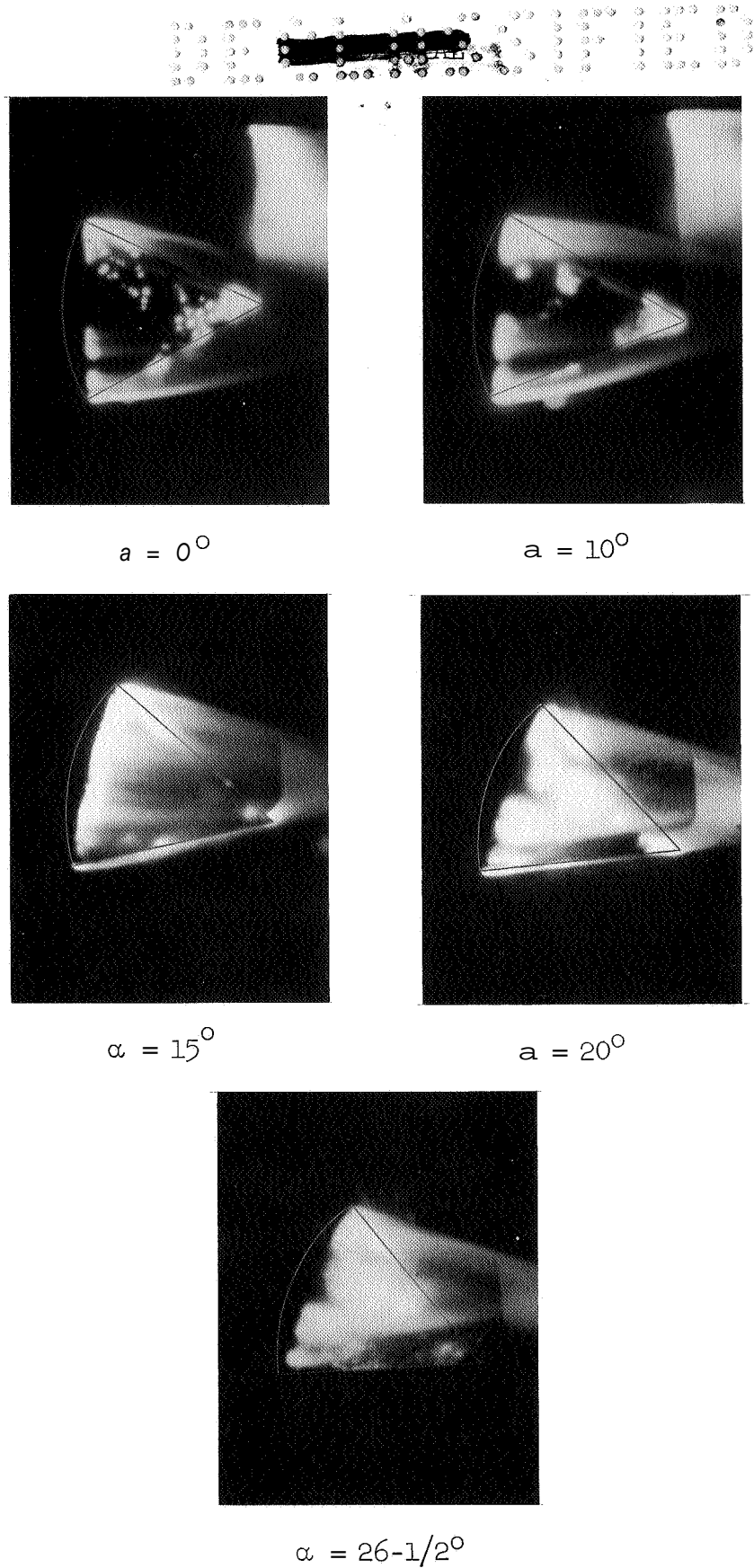


Figure 6.- Glow-discharge photographs of the flow over the afterbody for various angles of attack at $M_\infty = 15$.



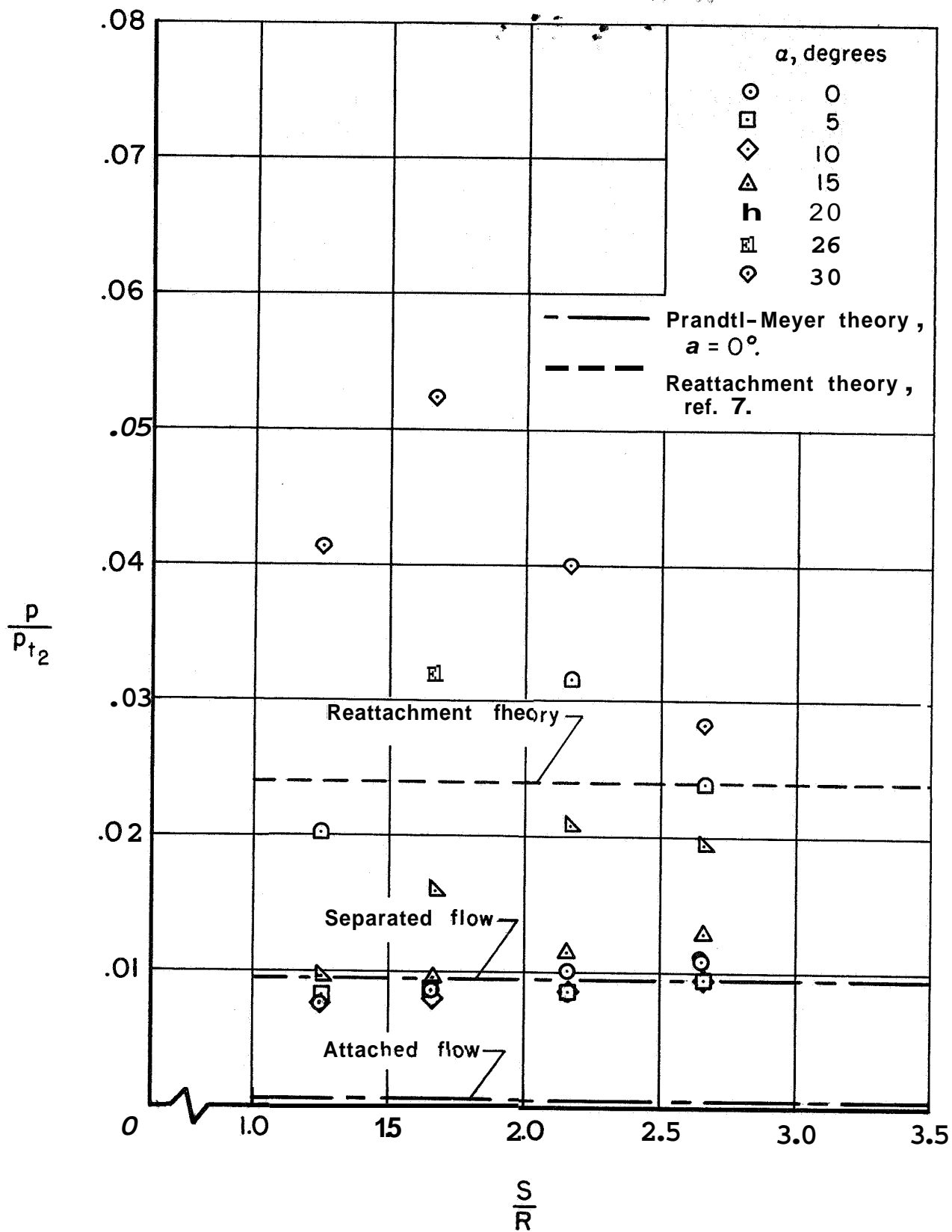
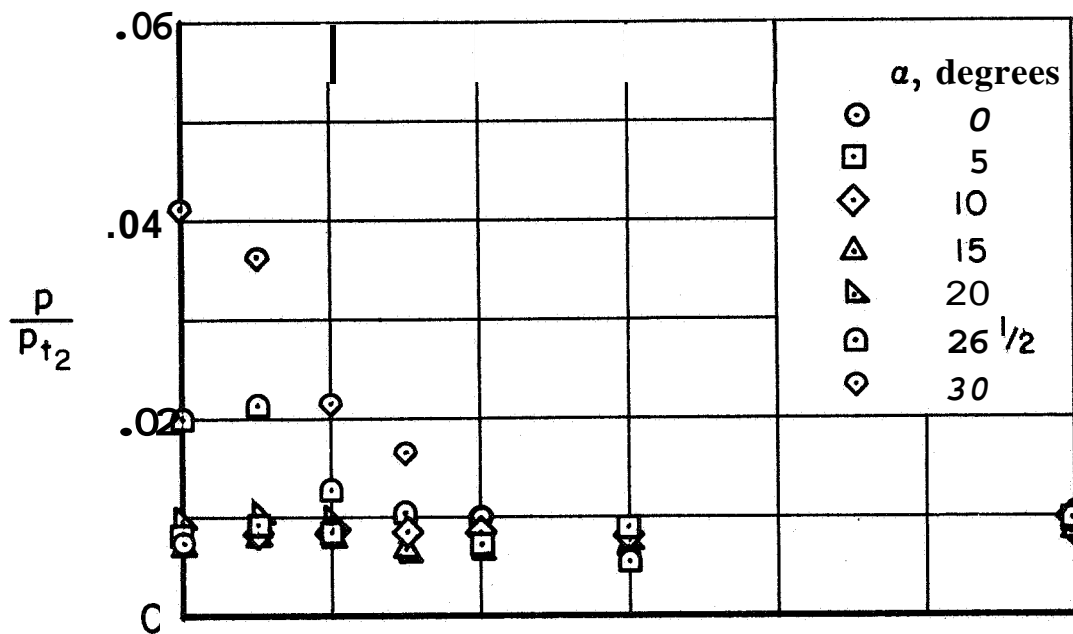
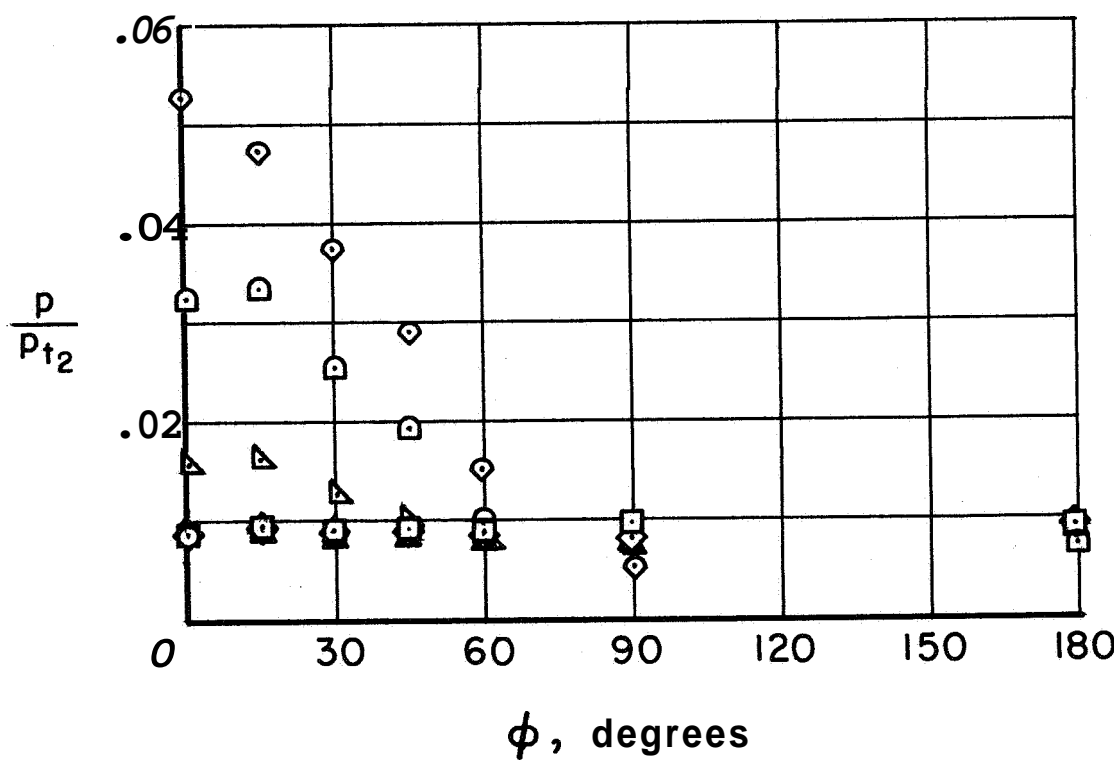


Figure 7.- Afterbody surface pressures along the most windward meridian for various angles of attack at $M_\infty = 15$.

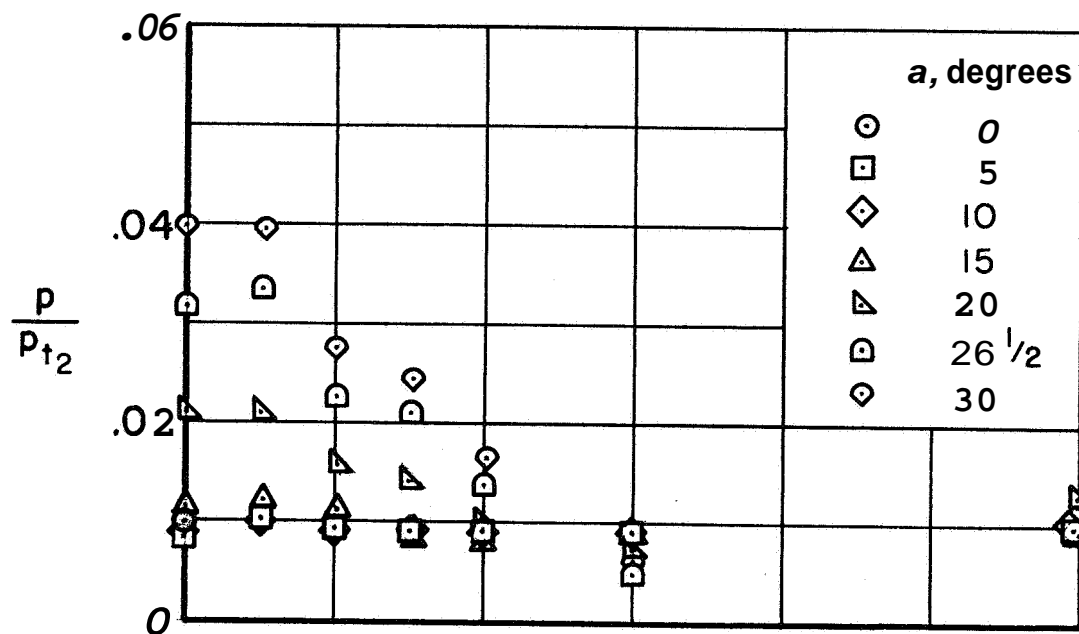


(a) $S/R = 1.251$

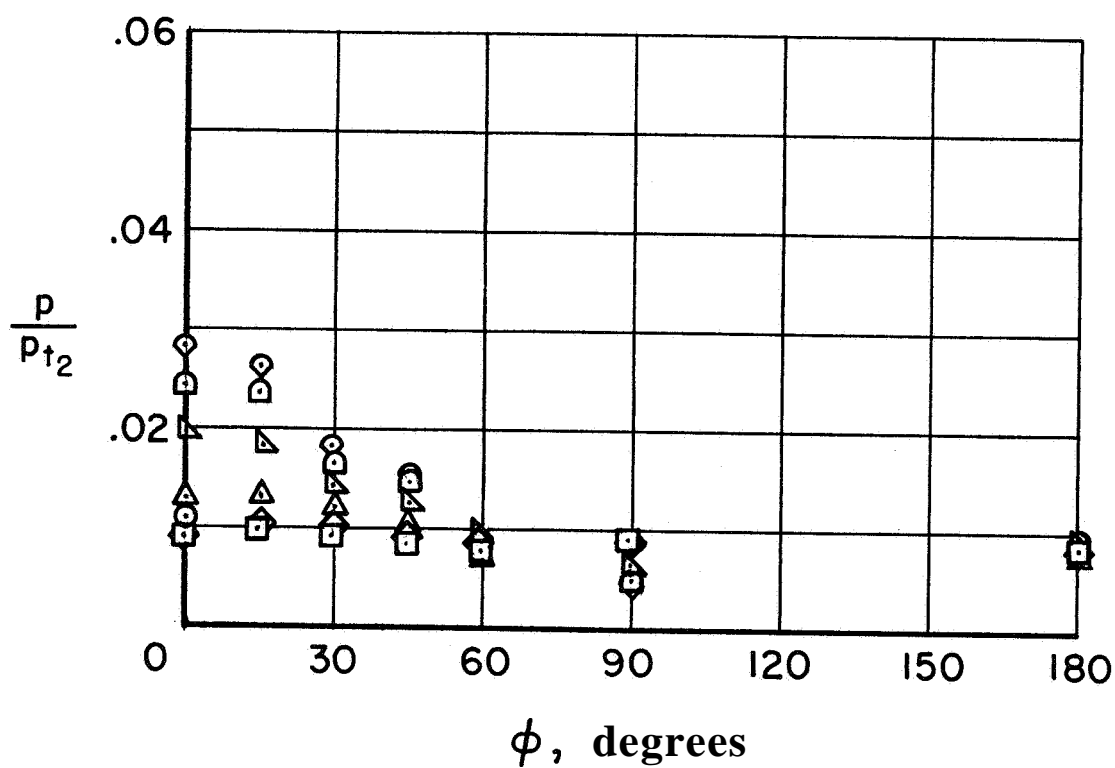


(b) $S/R = 1.651$

Figure 8.- Afterbody surface pressure variation with azimuth angle for various angles of attack at $M_\infty = 15$.

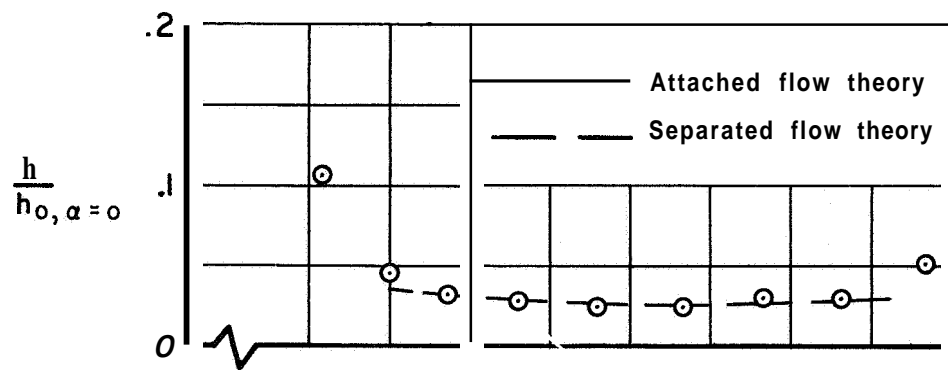


(c) $S/R = 2.151$

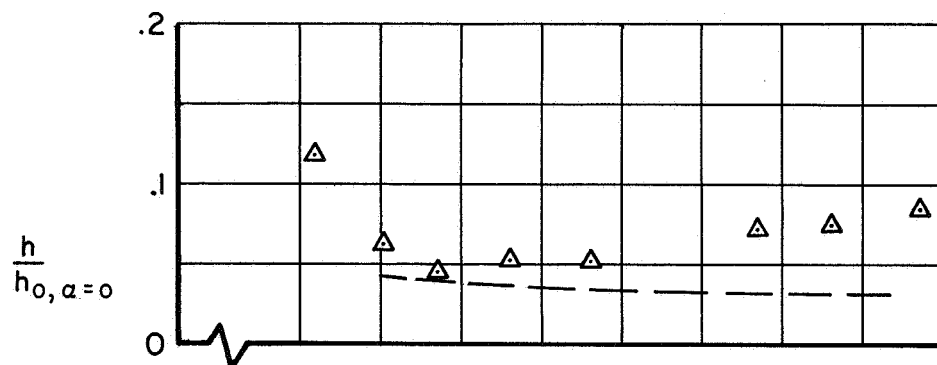


(d) $S/R = 2.651$

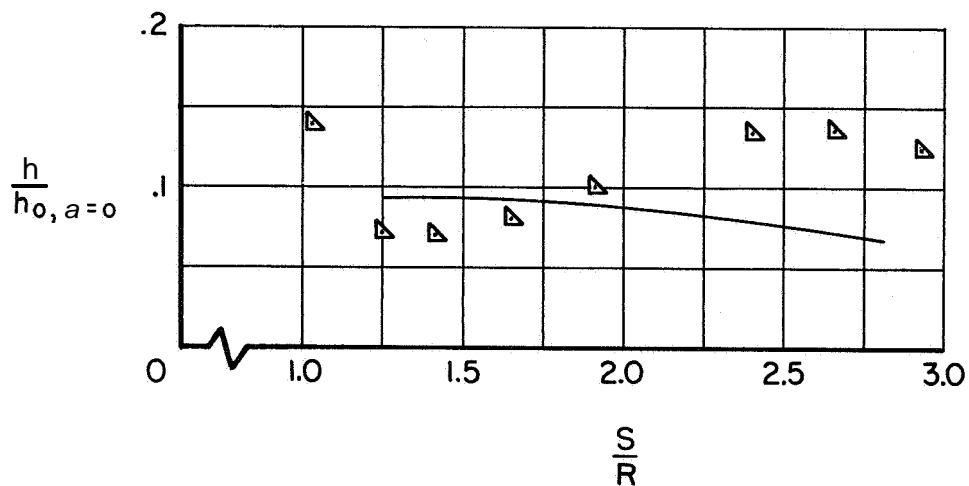
Figure 8. Concluded.



(a) $\alpha = 0^\circ$

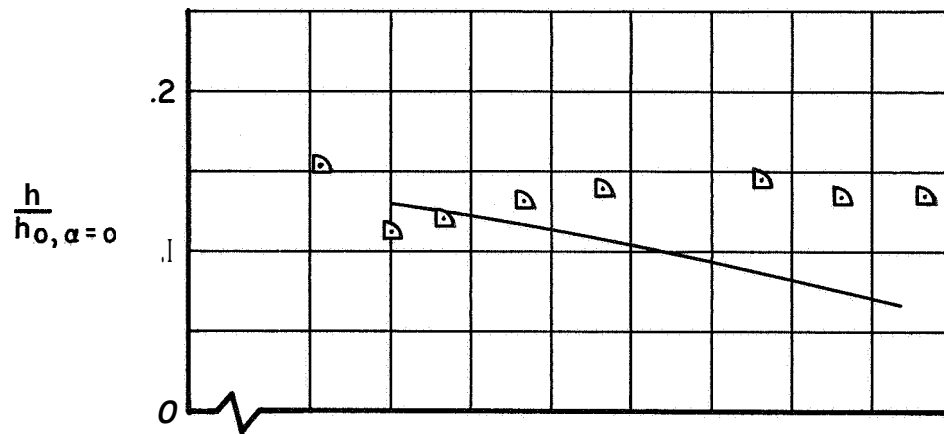


(b) $\alpha = 15^\circ$

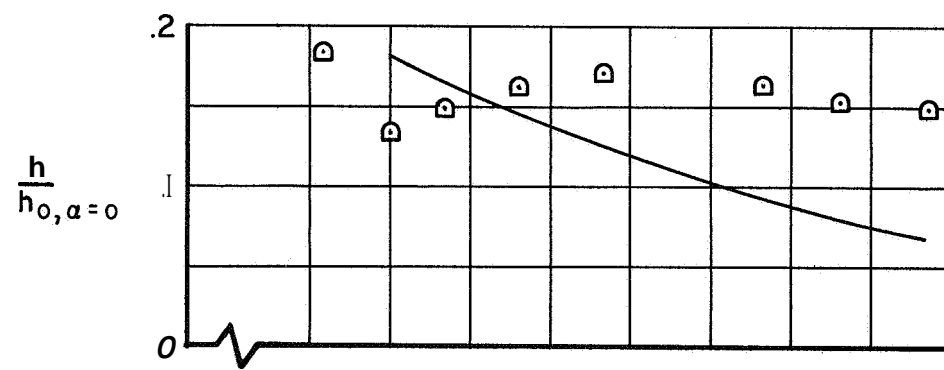


(c) $\alpha = 20^\circ$

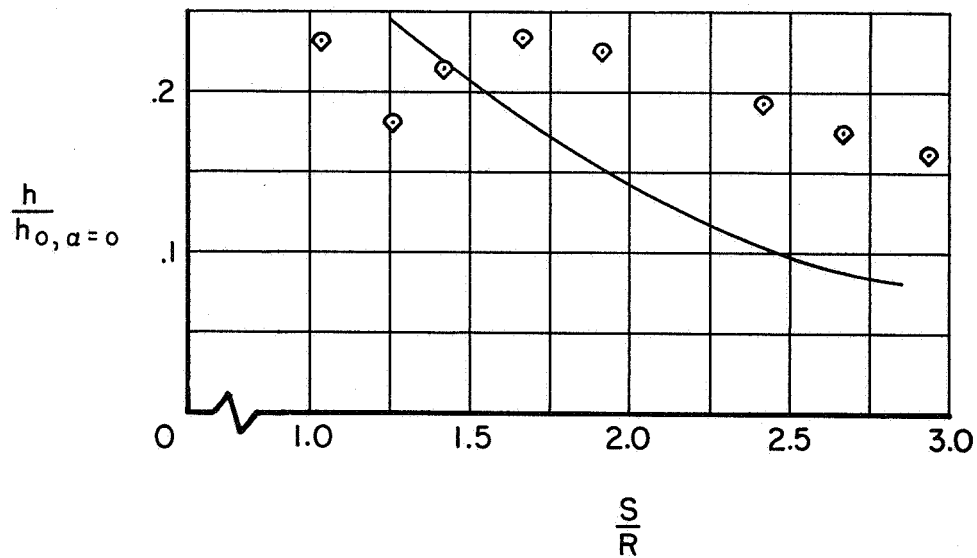
Figure 9.- Afterbody heat-transfer coefficients along the most windward meridian for various angles of attack at $M_\infty = 15$.



(d) $a = 23^\circ$

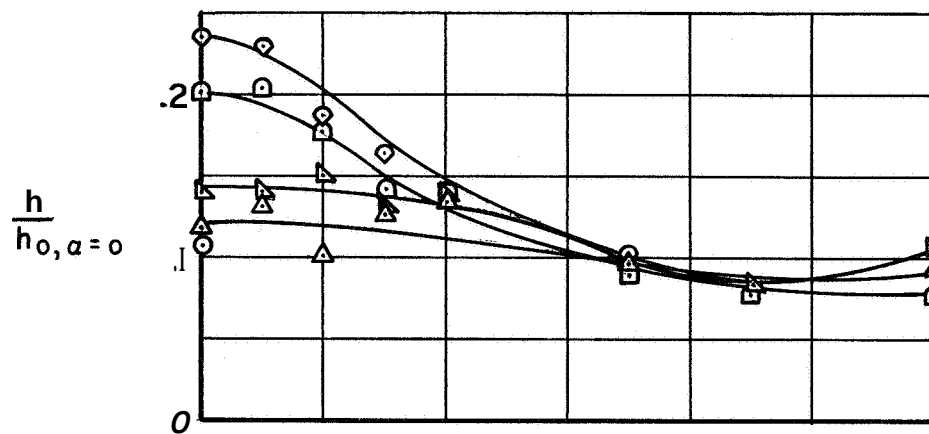


(e) $a = 26 \frac{1}{2}^\circ$

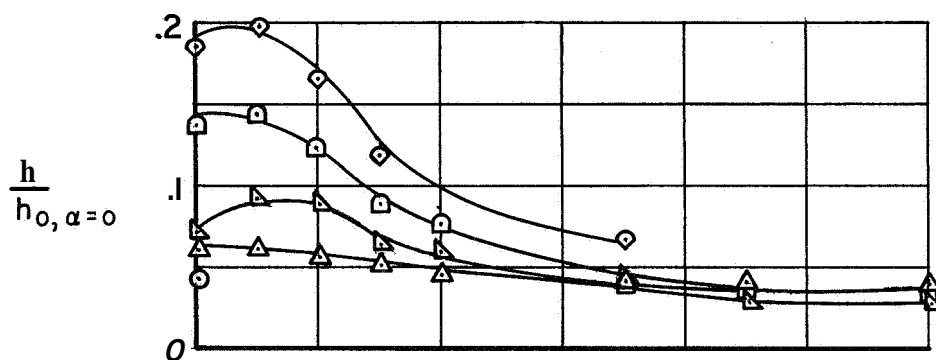


(f) $a = 30^\circ$

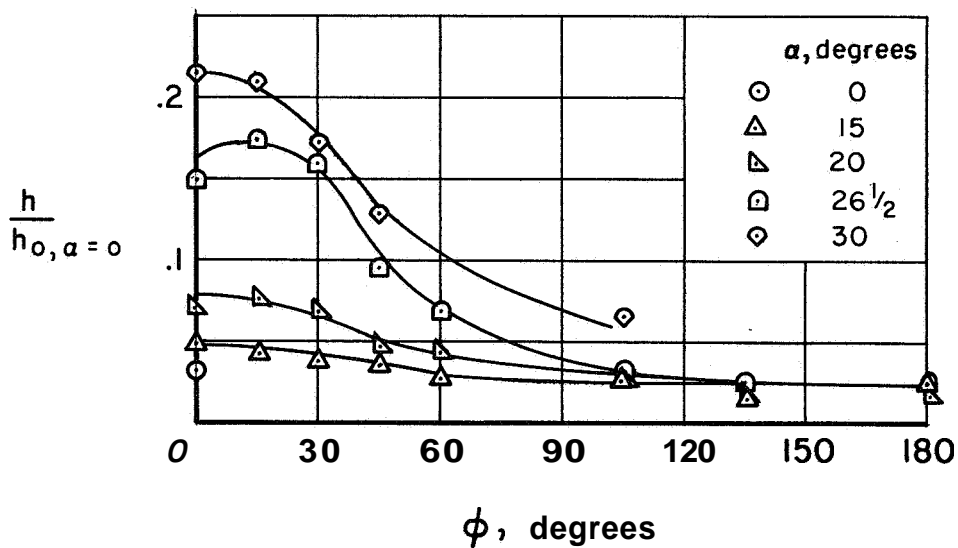
Figure 9.- Concluded.



(a) $S/R = 1.049$



(b) $S/R = 1.251$



(c) $S/R = 1.424$

Figure 10.—Afterbody heat-transfer coefficient variation with azimuth angle for various angles of attack at $M_\infty = 15$.

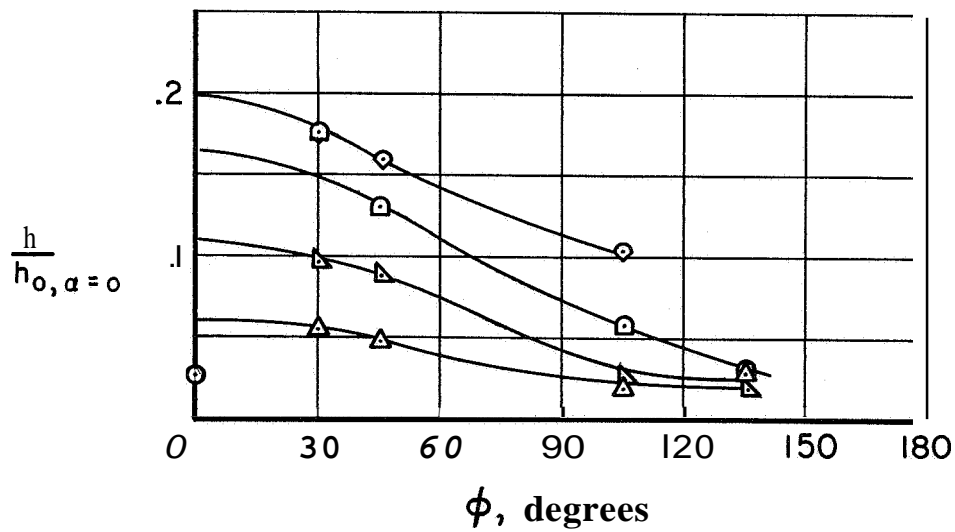
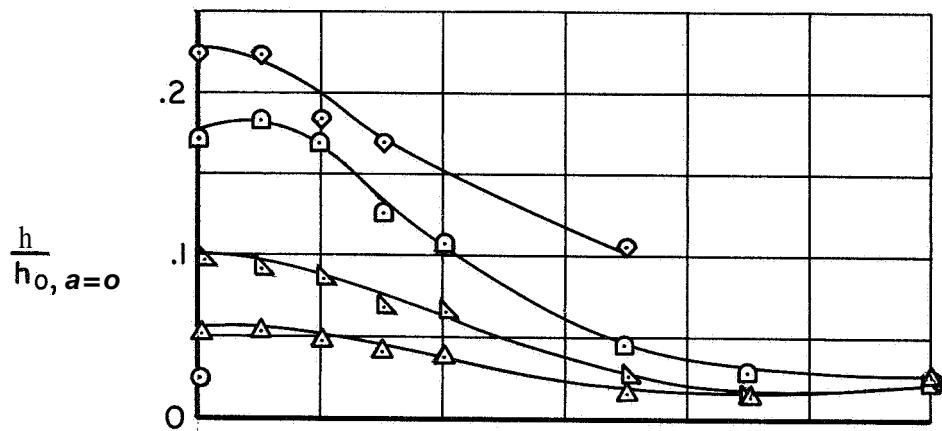
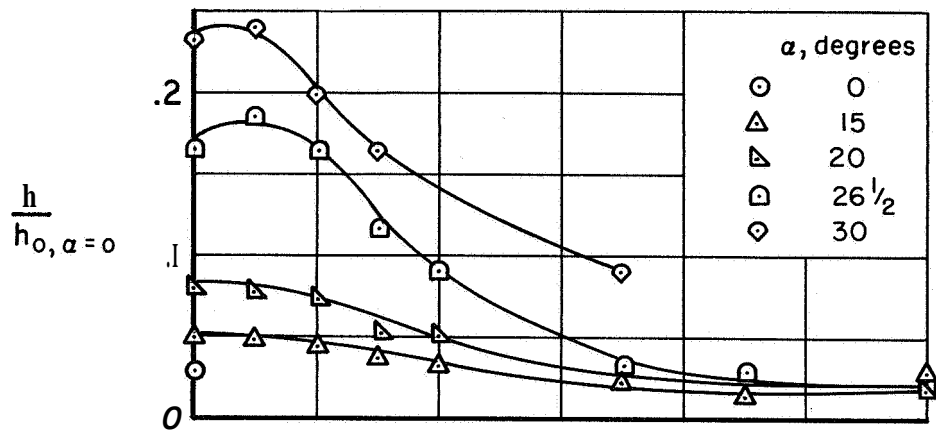
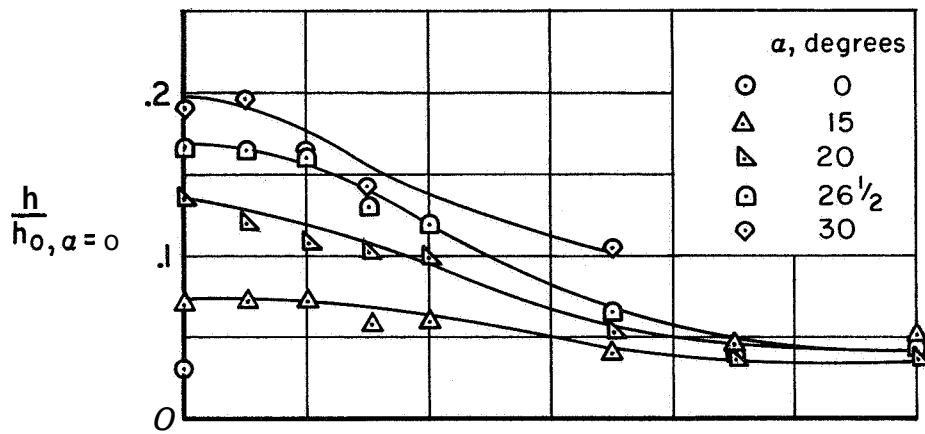
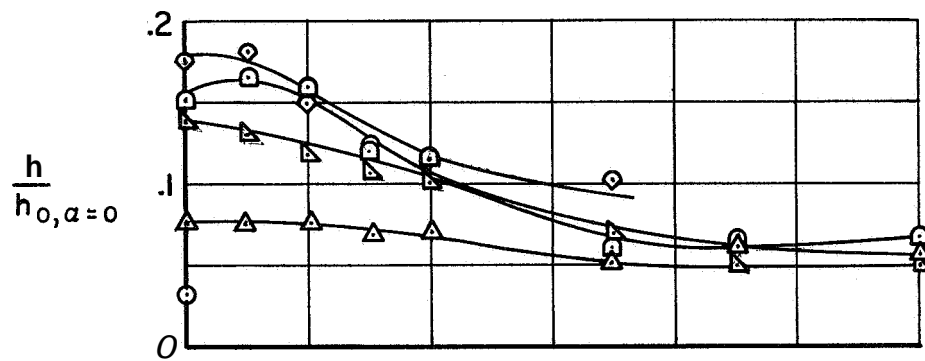


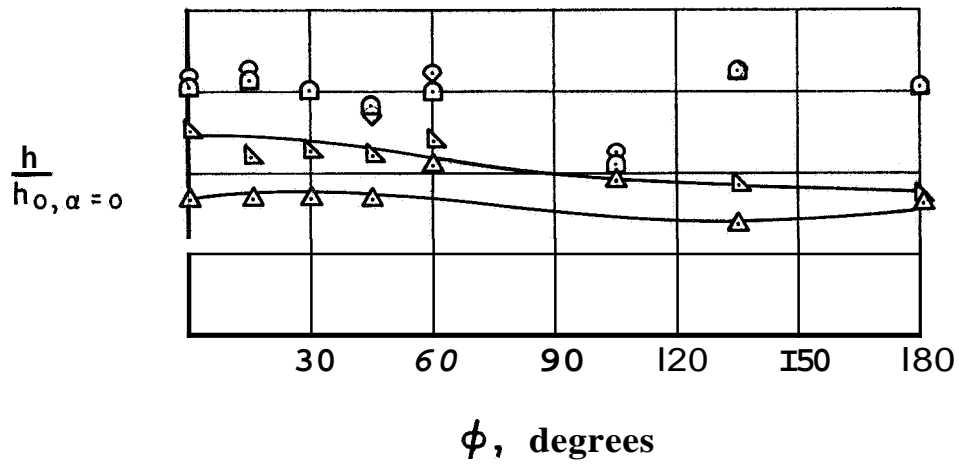
Figure 10.- Continued.



(g) $S/R = 2.424$



(h) $S/R = 2.651$

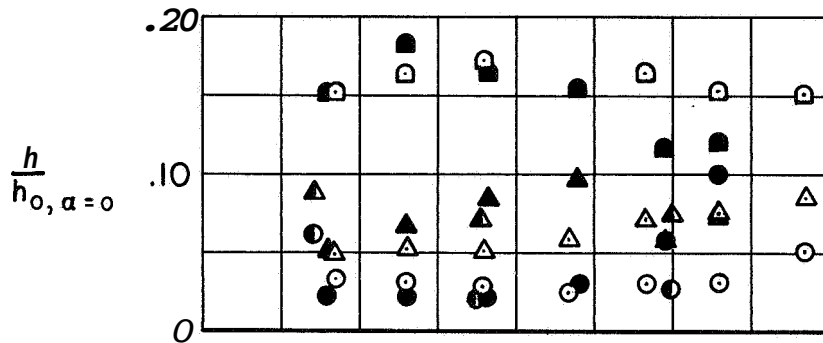


(i) $S/R = 2.924$

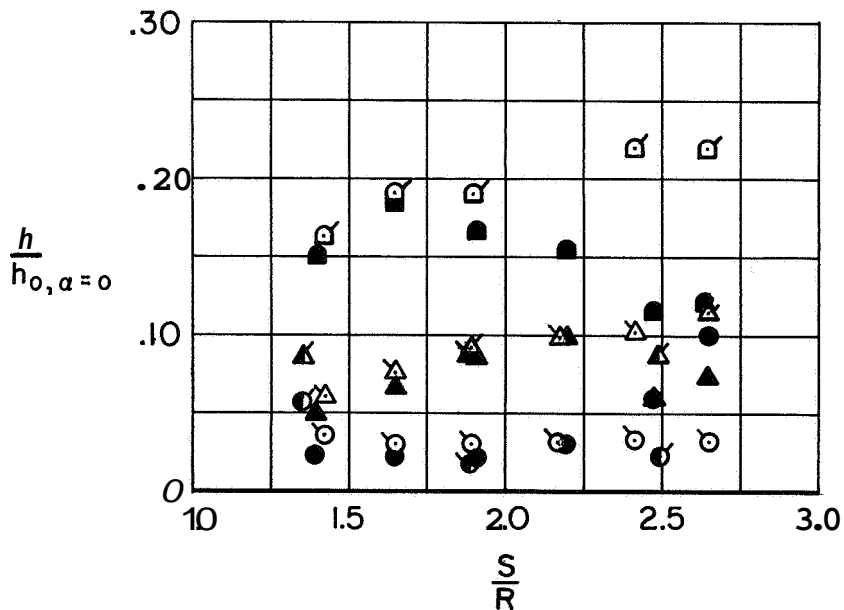
Figure 10.- Concluded.

	<u>a, degrees</u>	<u>ψ, degrees</u>	<u>Re_{D_2}</u>	<u>M_∞</u>	<u>Test gas</u>
⊙	0	$26\frac{1}{2}$	$.90 \times 10^5$	15	He
△	15	$9\frac{1}{2}$	$.90 \times 10^5$	15	He
◻	$26\frac{1}{2}$	0	$.90 \times 10^5$	15	He
●	0	20	1.55×10^5	8	Air (ref. 11)
▲	10	10	1.55×10^5	8	Air (ref. 11)
■	20	0	1.55×10^5	8	Air (ref. 11)
⊙	0	20	$.19 \times 10^5$	9.6	Air (ref. 12)
⊙	10	10	$.19 \times 10^5$	9.6	Air (ref. 12)

Note: Flagged symbols are adjusted data using eq. 9.



(a) Unadjusted data.



(b) Adjusted data, equation (9).

Figure 11. Comparison of afterbody heat-transfer coefficients measured in helium with those measured in air on a similar configuration.

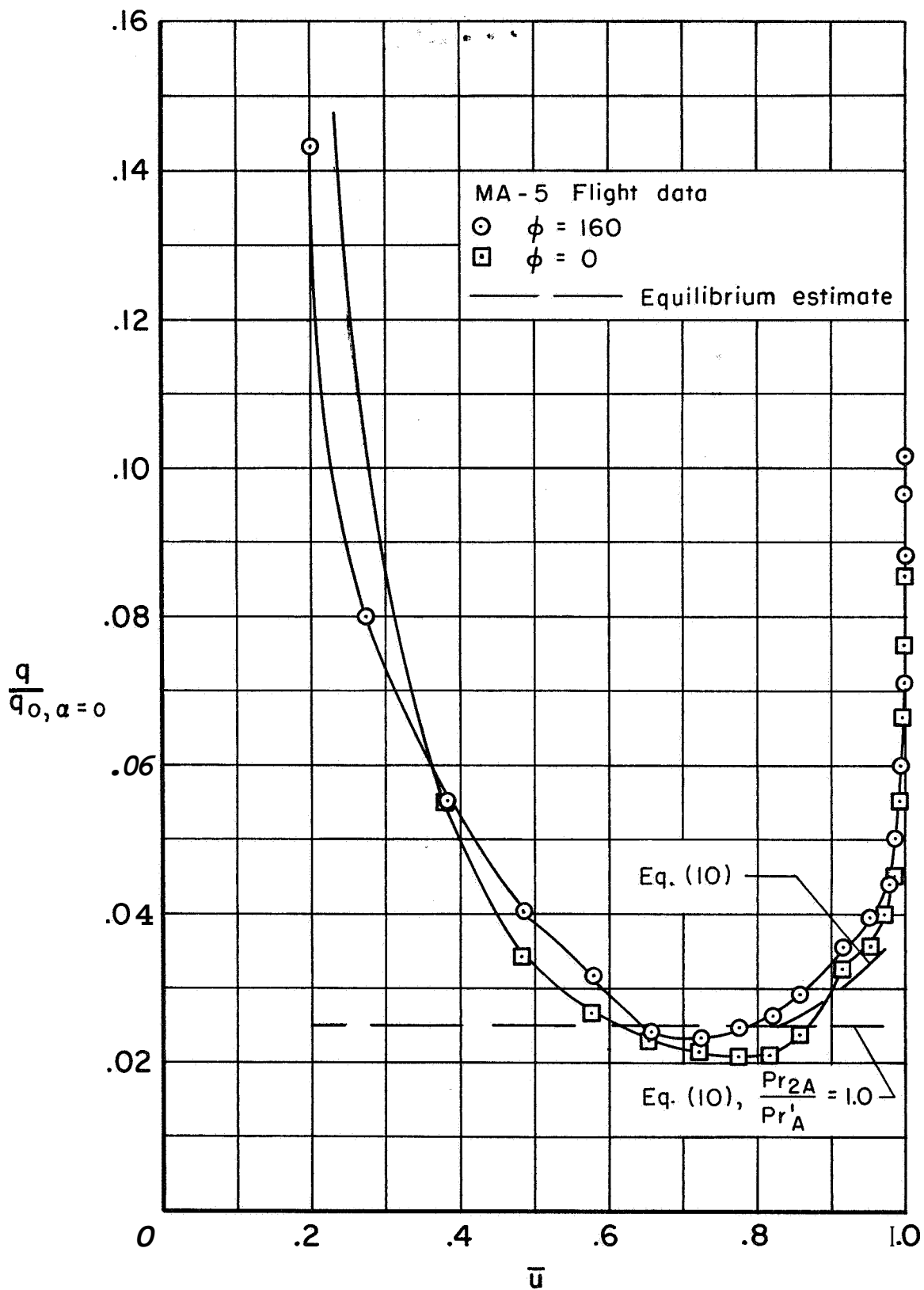


Figure 12.- Comparison of estimated heat transfer using wind-tunnel data with the MA5 flight data at $S/R = 1.67$.